# Statistical properties of the photoelectron energy spectrum generated by an intense laser pulse and a continuous X-ray*

Ge Yu-Cheng(葛愉成)†, Ge Xiang-Jie(葛湘洁), and He Hai-Ping(何海萍)

*School of Physics and State Key Laboratory of Nuclear Physics and Technology, Peking University, Beijing* 100871, *China*

(Received 23 April 2014; revised manuscript received 23 May 2014; published online 17 September 2014)

This study shows that the photoelectron energy spectrum generated by an intense laser pulse in the presence of a continuous X-ray has interesting and useful statistical properties. The total photoionization production is linearly proportional to the time duration of the laser pulse and the square of the beam size. The spectral double energy-integration is an intrinsic value of the laser-assisted X-ray photoionization, which linearly depends on the laser intensity and which quantitatively reflects the strengths of the laser-field modulation and the quantum interference between photoelectrons. The spectral energy width also linearly depends on the laser intensity. These linear relationships suggest new methods for the *in-situ* measurement of laser intensity and pulse duration with high precision.

**Keywords:** laser intensity, pulse duration, X-ray-boosted photoionization, statistical properties of photoelectron energy spectrum

**PACS:** 42.65.Re, 42.50.Hz, 42.50.Ct, 42.60.Jf **DOI:** 10.1088/1674-1056/23/11/114203

## 1. Introduction

In our recent work,[1] we studied laser-assisted X-ray photoionization and reported that an intense few-cycle laser pulse passing through a gas leaves a clear fingerprint of its field envelope on the photoelectron energy spectrum (PES), which involves continuous X-ray radiation. Figure 1(a) illustrates a typical experimental set-up for this laser pulse measurement. A linearly polarized few-cycle laser beam is focused to a small size and propagates in the $Z$ direction. The X-ray propagating in the $Y$ direction may be filtered from the Thomson scattering radiation,[2] or the high-order radiation generated by a synchronized picosecond intense laser (which is usually split from a primary beam before pulse compression).[3–5] The photoelectrons that leave the interaction region and fly in the $X$ direction are collected by an energy spectrometer. In a case where both the focused laser pulse and the X-ray co-linearly propagate in the $Z$ direction with an X-ray beam size much smaller than the laser, a PES $n(W)$ ($W$ denotes the photoelectron energy) like that shown in Fig. 1(c) (black solid line) can be measured. Here, the PES $n(W)$ is quantum-mechanically calculated using the strong field approximation.[1,6] Note that this PES has local peaks centered at spectral energy positions $W_{\rm a}$, $W_{\rm b}$, $W_{\rm c}$, etc. Because these energy positions correspond to the extremes of the laser electric field in the time domain, the peak data consist of a pulse fingerprint of the laser pulse envelope.

Analysis shows that the occurrence of the spectral fingerprint patten (Fig. 1(c)) can be attributed to the laser field modulation on the photoelectron energy and the quantum interference between photoelectrons generated at different times of the laser-assisted X-ray photoionizations.[7] The field modulation determines the overall spectral distribution with a clear energy coverage from $W_{\rm a-}$ to $W_{\rm b+}$, where $W_{\rm a-}$ is defined as a value slightly less than $W_{\rm a}$ and $W_{\rm b+}$ is defined as a value slightly greater than $W_{\rm b}$, see Fig. 1(c). While the quantum interference determines the local structures and fluctuations. The spectrum exhibits useful energetic properties. The spectral cut-off energies (e.g., $W_{\rm a}$ and $W_{\rm b}$ in Fig. 1(c)) reflect the strength, the time, and the interference of the laser field modulation. These energetic properties can be used for the precise *in-situ* measurement of the laser intensity.

Laser-assisted X-ray photoionization is significantly enhanced by the above threshold ionization (ATI),[8] which is called the X-ray-boosted photoionization (XBP).[1] The laser pulse in the XBP simply acts as a nonlinear photoelectron energy modulator, and the ATI is only a background of the XBP. The XBP has two advantages for the measurement of the laser intensity and pulse duration.

Firstly, the XBP spectrum can be easily identified from the ATI because the ATI probability of emitting high energy photoelectrons is much lower than the XBP. Physically, the ATI involves multi-photon ionization of atoms in a strong laser field. The ATI spectra have structural complications at low energies,[9] and the high harmonic spectra include contributions from electrons re-scattered from the parent ions with an energy coverage from $2U_{\rm p}$ to $10U_{\rm p}$, where $U_{\rm p}$ is the electron's ponderomotive energy in the laser field.[10] In contrast, the XBP spectrum is centered at the energy of $\omega_{\rm X} - I_{\rm p}$, where $\omega_{\rm X}$ is the angular frequency of the X-ray, and $I_{\rm p}$ is the atomic ionization potential of the active gas. Usually, $\omega_{\rm X} - I_{\rm p}$ is much

*Project supported by the National Natural Science Foundation of China (Grant No. 11175010).

†Corresponding author. E-mail: gyc@pku.edu.cn

© 2014 Chinese Physical Society and IOP Publishing Ltd 

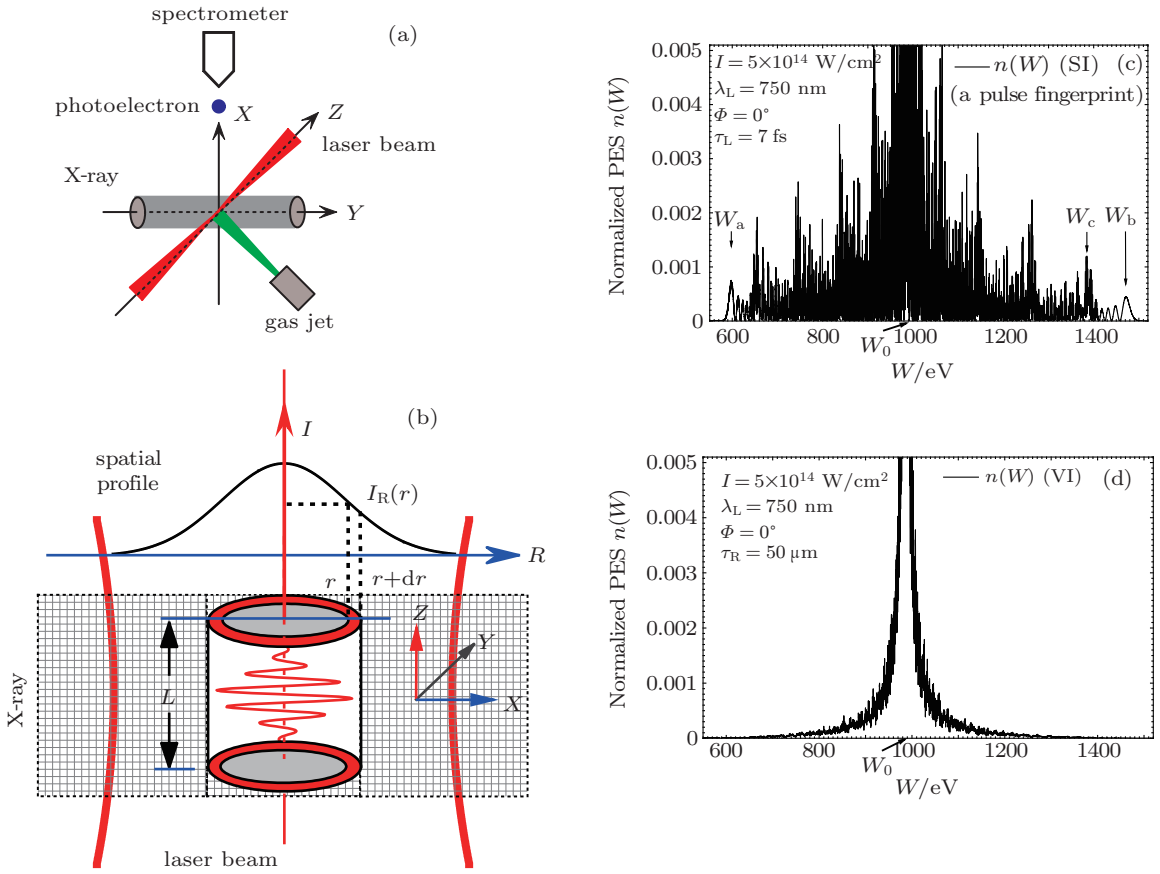



**Fig. 1.** (color online) Illustrations of the XBP set-up and normalized photoelectron energy spectra. (a) The 90°-correlation between an X-ray and a laser pulse. The X-ray propagating in the $Y$ direction may be filtered from the Thomson scattering radiation,[2] or the high-order radiation generated by a synchronized picosecond intense laser (which is usually split from a primary beam before pulse compression).[3–5] The photoelectrons that leave the interaction region and fly in the $X$ direction are collected by a photoelectron detector (spectrometer). (b) A spatial profile of the laser intensity, $I_R(r) = \exp[-4\ln 2(r)^2/\tau_R^2]$ (black curve), and an iso-intensity shell in the interaction volume (radius $r$, thickness $dr$, and length $L$.) (c) SI data based on $n(W)$ (normalized), a fingerprint of the laser pulse. (d) VI $n(W)$ data (normalized) calculated using $\tau_R = 50$ μm.

greater than $10U_p$ for the laser intensities concerned.[1] Even if the momentum shift of the photoelectron in the laser field is considered, the lower limit of the photoelectron energy, which is classically about $(\omega_X - I_p) - \sqrt{8U_p(\omega_X - I_p)}$ or quantum-mechanically $W_a$ (Fig. 1(c)), is still much higher than $10U_p$ for keV X-rays and intermediate laser intensities ($I < 10^{15}$ W/cm$^2$ and $U_p < 52.524$ eV for 750 nm laser).

Secondly, the XBP spectrum has linear features that are different from the ATI spectra. For example, calculations show that the spectral values are proportional to the X-ray intensity $I_X$, and the spectral energy width (i.e., the spectral energy coverage) is proportional to the square root of the laser intensity $I$. These interesting spectral features lead us to further study the statistical properties of the XBP photoelectron energy spectrum (XBP PES) and its use for the *in-situ* measurement of a strong laser pulse.

For different spatial configurations between laser pulse and X-ray, the XBP PES is classified as single-intensity (SI) or volume-integral (VI)[1], depending on whether it is calculated (measured) by excluding or including, respectively, the contributions from laser intensity less than $I$. The SI PES data (e.g., the PES shown in Fig. 1(c)) can be obtained by a 0°-correlation measurement in which a smaller X-ray is intensity-uniformly dressed by the laser beam (i.e., co-linear mode), while the VI data can be obtained by either a 0°-correlation measurement (i.e., co-linear mode with spatially uniform X-ray intensity within the laser beam size) or a 90°-correlation measurement (i.e., orthogonal mode, e.g. Fig. 1(a)). We note that the SI spectral fingerprint patten for a strong few-cycle laser disappears in the VI measurement (the PES (solid line) shown in Fig. 1(d)). Therefore, analyzing the XBP statistical properties serves a new approach for the VI laser pulse measurement.

The use of the XBP statistical properties can improve the precision of atto- and femto-second X-ray pulse measurements. In our previous works,[11–15] we have established three transfer equations for the measurement of atto- and femtosecond X-ray pulses using laser-assisted photoionizations. For simplicity, the equations have the forms of (i) $f(t) = \mu_1 n(W) \cdot dW(t)/dt$, $dW(t)/dt = \omega_L\sqrt{8U_p(\omega_X - I_p)}F(t)\cos(\omega_L t + \Phi)$ for the attosecond measurement, and (ii) $f(t) = \mu_2 U_p \times$

$\mathrm{d}F^2(t)/\mathrm{d}t \cdot \mathrm{d}n(V)/\mathrm{d}t$, $\mathrm{d}V(t)/\mathrm{d}t = 2\sqrt{U_\mathrm{p}}\mathrm{d}F(t)/\mathrm{d}t$ for the femtosecond measurement. Here, $\mu_1$ and $\mu_2$ are two constant factors that can be set to 1, $f(t)$ represents the pulse temporal profile to be measured for the attosecond or femtosecond X-ray pulse, and $n(W)$ and $n(V)$ are the measured photoelectron energy ($W$) spectrum and the measured photoelectron velocity ($V$) spectrum, respectively. The $F(t) = \exp(-4\ln 2 \cdot t^2/\tau_\mathrm{L}^2)$ is a Gaussian-like time function describing the laser pulse envelope, and $\omega_\mathrm{L}$, $\Phi$, and $\tau_\mathrm{L}$ represent the angular frequency, the carrier-envelope phase, and the pulse duration (in full-width-at-half-maximum, FWHM) of the laser pulse, respectively. Note that $\sqrt{U_\mathrm{p}}$ directly occurs in the time derivatives $\mathrm{d}(W)/\mathrm{d}t$ and $\mathrm{d}V(t)/\mathrm{d}t$, and $U_\mathrm{p}$ occurs in the transfer equation, where $U_\mathrm{p} = I/2\omega_\mathrm{L}^2 \propto I$ is the ponderomotive energy of electron in the laser field. Therefore, the results and the precision of the atto- and femto-second X-ray measurements depend directly on those of the laser intensity ($I$) measurement. Particularly, we can benefit from the *in-situ* measurement of the intensity of the laser pulse.

The rest of this paper is organized as follows. In Section 2, some variants and invariants that characterize the XBP statistical properties, such as the photoionization production and the spectral double energy integral, are defined. In Section 3, the linear relationships between the XBP statistical properties and the laser parameters are presented for pulse measurement. Finally, we summarize our investigations in Section 4.

## 2. XBP's statistical properties

There is no clear fingerprint pattern for a long laser pulse or when a VI PES is measured; we must therefore extract the pulse information from the statistical properties of the PES. Some invariants and linear relationships between the XBP statistical properties and the laser parameters greatly simplify the measurement algorithm.

### 2.1. SI and VI $Q$ values

For either SI data (e.g., the PES $n(W)$ in Fig. 1(c)) or VI data (e.g., the PES $n(W)$ in Fig. 1(d)), $Y$ is defined as the total yield of the XBP,

$$Y \equiv \int_{W_{\mathrm{a}-}}^{W_{\mathrm{b}+}} n(W)\mathrm{d}W - \int_{W_{0-}}^{W_{0+}} n(W)\mathrm{d}W, \tag{1}$$

where $W_{\mathrm{a}-}$ and $W_{\mathrm{b}+}$ are measured lower and upper spectral cut-off energies, respectively, and $W_{0-} = 984$ eV and $W_{0+} = 989$ eV for $\omega_\mathrm{X} = 1$ keV X-rays. Here, the photoelectrons with energies within the bandwidth (centered at $W_0 = 986.4$ eV) ranging from $W_{0-}$ to $W_{0+}$ are removed because they are indistinguishable from those generated in the region where $I \approx 0$ and those generated in the absence of the laser pulse. The normalized and energy-integrated spectrum of an XBP PES $n(W)$ is defined as

$$y(W) \equiv \int_{W_{\mathrm{a}-}}^{W} \mathrm{d}W n(W)/Y, \tag{2}$$

where $n(W)$ is set to 0 for $W_{0-} < W < W_{0+}$. The S-like dotted and solid lines in Fig. 2(a) show the calculated SI and VI values of $y(W)$, respectively. Because $n(W)$ exhibits complicated structures due to the quantum interference and the path of $y(W)$ in the energy space changes as $I$ varies, we define an observable value $Q$,

$$\begin{aligned} Q &\equiv \int_{W_{0+}}^{W_{\mathrm{b}+}} q(W)\mathrm{d}W \\ &= \int_{W_{0+}}^{W_{\mathrm{b}+}} \mathrm{d}W \int_{W}^{W_{\mathrm{b}+}} \mathrm{d}W' n(W')/Y, \end{aligned} \tag{3}$$

where $q(W) \equiv \int_{W}^{W_{\mathrm{b}+}} \mathrm{d}W' n(W')/Y = 1 - y(W)$ is integrated from $W_{0+}$ to $W_{\mathrm{b}+}$. The $Q$ is a path-energy integral of $1 - y(W)$. The area of the shaded region in Fig. 2(a) (denoted as $Q_\mathrm{VI}$) represents the value of $Q$. Obviously, $Q$ is in units of eV. The $Y$ and $Q$ are useful for describing the statistical properties of the XBP.

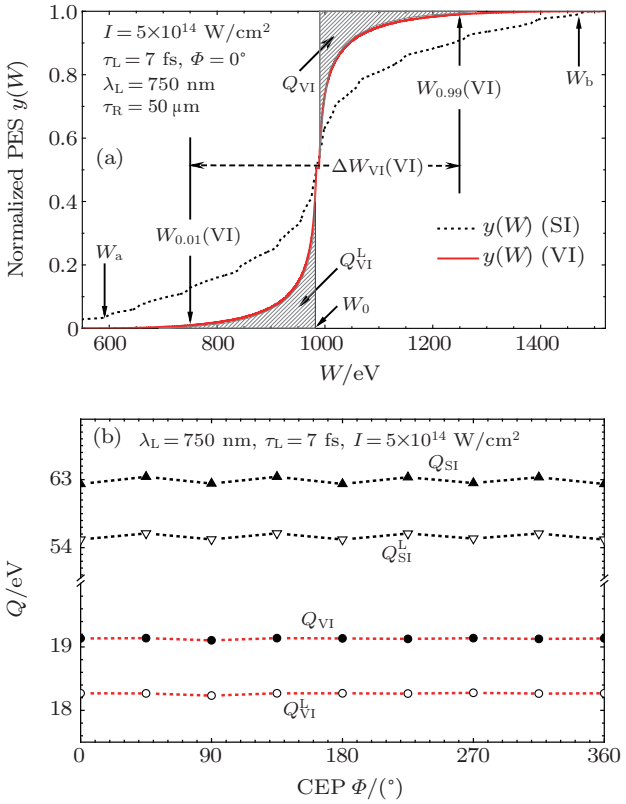



**Fig. 2.** (color online) XBP statistical properties. (a) Normalized and energy-integrated XBP PES. Solid line: VI data corresponding to $y(W) = \int^{W} \mathrm{d}W' n(W')/Y$ ($\tau_\mathrm{R} = 50$ μm). Dotted line: SI data corresponding to $y(W) = \int_{W_{\mathrm{a}-}}^{W} \mathrm{d}W' n(W')/Y$. The areas of the shaded regions represent the values of $Q_\mathrm{VI}$ and $Q^\mathrm{L}_\mathrm{VI}$. (b) Open (filled) circles: VI data corresponding to $Q^\mathrm{L}_\mathrm{VI}$ ($Q_\mathrm{VI}$) versus $\Phi$. Open (filled) triangles: SI data corresponding to $Q^\mathrm{L}_\mathrm{SI}$ ($Q_\mathrm{SI}$) versus $\Phi$.

Similarly, we can define another observable value $Q^{\rm L}$,

$$Q^{\rm L} \equiv \int_{W_{\rm a-}}^{W_{0-}} y(W)\,{\rm d}W = \int_{W_{\rm a-}}^{W_{0-}} {\rm d}W \int_{W_{\rm a-}}^{W} {\rm d}W' n(W')/Y, \quad (4)$$

where $y(W) \equiv \int_{W_{\rm a-}}^{W} {\rm d}W' n(W')/Y$ is integrated from $W_{\rm a-}$ to $W_{0-}$. The $Q^{\rm L}$ is another path-energy integral of $y(W)$. The area of the shaded region in Fig. 2(a) (denoted as $Q^{\rm L}_{\rm VI}$) represents the value of $Q^{\rm L}$. If the ATI spectrum $n_{\rm L}(W)$ can be neglected in comparison with the XBP PES $n(W)$, then $Q^{\rm L}$ is as useful as $Q$ (Eq. (3)) for describing the XBP statistical properties. However, the low energy portion of $n(W)$ ($W < W_0$) may be polluted by the ATI if the laser intensity is high enough, and the calculated or measured $Q^{\rm L}$ may include errors.

Similar to the calculation of $Q_{\rm VI}$ and $Q^{\rm L}_{\rm VI}$, we can calculate SI $Q$ values from an SI XBP PES $n(W)$: $Q_{\rm SI}$ and $Q^{\rm L}_{\rm SI}$ (Eqs. (3) and (4)). Figure 2(b) shows some VI and SI data corresponding to $Q_{\rm VI}$, $Q^{\rm L}_{\rm VI}$, $Q_{\rm SI}$, and $Q^{\rm L}_{\rm SI}$ that have been calculated with $\lambda_{\rm L} = 750$ nm, $\tau_{\rm L} = 7$ fs, $I = 5 \times 10^{14}$ W/cm$^2$, and $\Phi = 0°$–$360°$. The plots show that: (i) the SI $Q$ values are greater than the VI $Q$ values, (ii) $Q > Q^{\rm L}$ for both the SI and the VI PES, and (iii) all $Q$ values remain nearly unchanged as $\Phi$ varies from 0° to 360°. The following features are useful for measurements: (i) $Q$ and $Q^{\rm L}$ have the same status, and (ii) $Q$ and $Q^{\rm L}$ are almost independent of $\Phi$.

### 2.2. Invariants and slow variables

To discuss the XBP statistical properties, we use invariants and slow variables to simplify the algorithm and the difficulties in the quantitative analysis of the experimental data.

#### 2.2.1. XBP's production $Y$

The open (filled) circles in Fig. 3(a) present the SI (VI) XBP productions corresponding to $Y_{\rm SI}$ ($Y_{\rm VI}$) versus $\Phi$. Both $Y_{\rm SI}$ and $Y_{\rm VI}$ remain nearly unchanged as $\Phi$ varies; that is, they can be regarded as invariants for different CEP $\Phi$. The open (filled) circles in Fig. 3(b) show the SI (VI) XBP productions corresponding to $Y_{\rm SI}$ ($Y_{\rm VI}$) versus $I$. According to the linearly fitted lines, both $Y_{\rm SI}$ and $Y_{\rm VI}$ increase slowly as $I$ increases from $10^{12}$ W/cm$^2$ to $1.5 \times 10^{15}$ W/cm$^2$. The $Y_{\rm SI}$ and $Y_{\rm VI}$ are regarded as slow variables. Over a limited laser intensity range, they can be regarded as invariants. A quantitative analysis shows that the change in $Y$ with increasing laser intensity $I$ is a result of the change in the ATI. The CEP independence of $Y$ and the weak intensity dependence of $Y$ indicate that: (i) the field modulation and the interference in the XBP affect the spectral distribution, including the fine structures and the local fluctuations, but not the total production, and (ii) the ATI contribution is a background of the $Y$ measurement, which increases as the laser intensity $I$ increases.

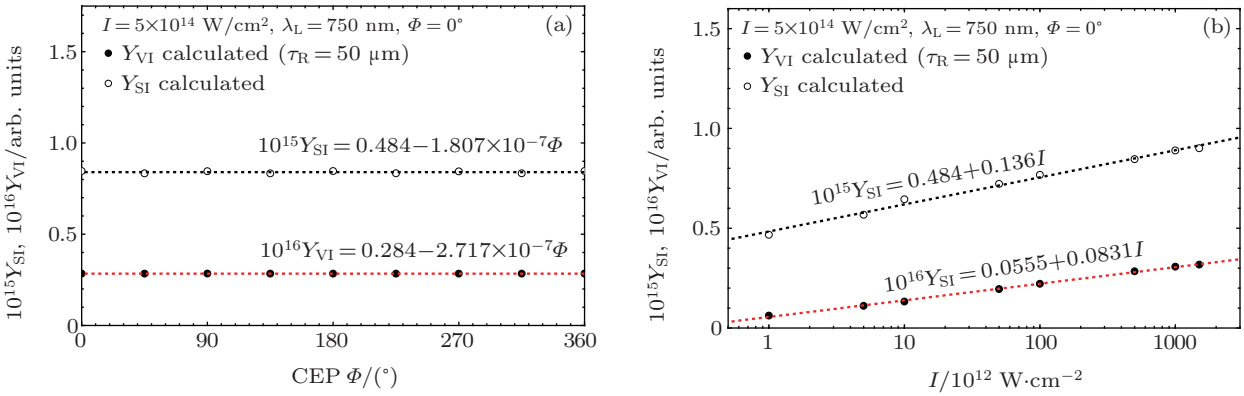



**Fig. 3.** (color online) XBP production $Y$. (a) CEP-independence of $Y$. Open (filled) circles: $Y_{\rm SI}$ ($Y_{\rm VI}$) versus $\Phi$. Lines are linearly fitted from $Y_{\rm SI}$ and $Y_{\rm VI}$. (b) Intensity-dependence of $Y$. Open (filled) circles: $Y_{\rm SI}$ ($Y_{\rm VI}$) versus $I$. Lines are linearly fitted from $Y_{\rm SI}$ and $Y_{\rm VI}$.

#### 2.2.2. XBP's $Q$ value

Figures 4(a)–4(c) show SI and VI XBP $Q$ values calculated with $\lambda_{\rm L} = 750$ nm, $\tau_{\rm L} = 7$ fs, $I = 5 \times 10^{14}$ W/cm$^2$, $\omega_{\rm X} = 1$ keV and different $\Phi$, $\tau_{\rm L}$, and $\tau_{\rm R}$. According to the linearly fitted lines, the $Q$ values remain nearly unchanged as $\Phi$, $\tau_{\rm L}$, and $\tau_{\rm R}$ increase. For example, the mean value of $Q_{\rm SI}$ ($Q_{\rm VI}$) for $\Phi = 0°$–$360°$ (Fig. 4(a)) is $\bar{Q}_{\rm SI} = 62.853$ eV ($\bar{Q}_{\rm VI} = 19.130$ eV), and the relative difference is $\delta Q_{\rm SI} \equiv |Q_{\rm SI} - \bar{Q}_{\rm SI}|/Q_{\rm SI} < 0.830\%$ ($\delta Q_{\rm VI} \equiv |Q_{\rm VI} - \bar{Q}_{\rm VI}|/Q_{\rm VI} < 0.139\%$). Calculations with different laser intensities $I$ reveal the same conclusion. The $\Phi$-, $\tau_{\rm L}$-, and $\tau_{\rm R}$-independences indicate that $Q$ describes the overall spectral distribution but not the local spectral structures and fluctuations.

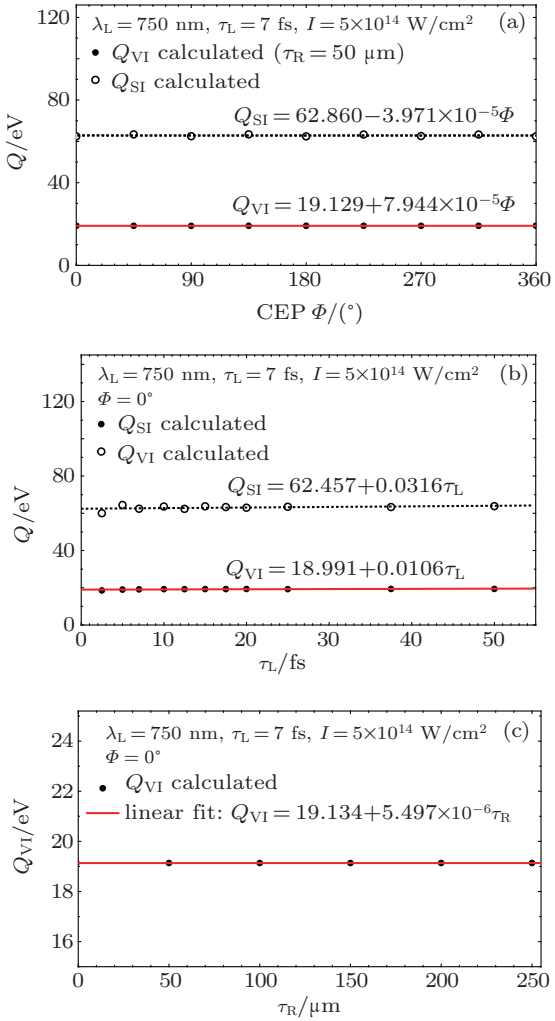



**Fig. 4.** (color online) XBP $Q$ values. (a) CEP-independence of $Q$. Open (filled) circles: SI (VI) data corresponding to $Q_{\rm SI}$ ($Q_{\rm VI}$) versus $\Phi$. Lines are linearly fitted from $Q_{\rm SI}$ and $Q_{\rm VI}$. (b) The $\tau_{\rm L}$-independence of $Q$. Open (filled) circles: SI (VI) data corresponding to $Q_{\rm SI}$ ($Q_{\rm VI}$) versus $\tau_{\rm L}$. Lines are linearly fitted from $Q_{\rm SI}$ and $Q_{\rm VI}$. (c) The $\tau_{\rm R}$-independence of $Q$. Filled circles: VI data corresponding to $Q_{\rm VI}$ versus $\tau_{\rm R}$. The line is linearly fitted from $Q_{\rm VI}$.

## 3. Linear relationships for laser pulse measurement

The linear relationships between the statistical properties of the PES and the laser pulse parameters can be derived from the detector configurations and the measured PES. We consider an iso-intensity shell (radius $r$, with $r < R$, $R$ being the radius of the laser beam, $R \propto \tau_{\rm R}$, thickness d$r$, length $L$, shell volume $2\pi r{\rm d}rL$; as shown in Fig. 1(b)) and the detector configurations (geometric factor $g$, detection efficiency $\eta$, atomic density $\rho$), the number of generated photoelectrons with energy $W$ is

$$ {\rm d}N(W) = \kappa \cdot g\eta\rho \cdot 2\pi r{\rm d}rL \cdot n_{\rm r}(W){\rm d}W, \tag{5} $$

where $\kappa$ is a constant and $n_{\rm r}(W)$ is an SI PES produced in the shell. Our calculations show that: (i) the SI photoelectron production, $Y_{\rm SI} \equiv \int n_{\rm r}(W){\rm d}W$, is a constant for different laser intensities $I$ and CEPs $\Phi$, and (ii) $Y_{\rm SI} \propto \tau_{\rm L}$. Both (i) and (ii) can be understood through the mechanism of laser field modulation. Although the XBP PES includes fine structures and local fluctuations, the total XBP production depends on the time duration of the laser vector potential $\boldsymbol{A}_{\rm L}(t) \neq 0$ (i.e., $I \neq 0$), during which the photoelectrons excited by the X-ray are pumped from energy $W_0$ to $W \neq W_0$. Obviously, this time is proportional to the pulse duration $\tau_{\rm L}$, and it is independent of $I$ and CEP $\Phi$. Energy-integrating d$N(W)$ and space-integrating d$N(W)$ over radius $r$ from 0 to $R$ gives the total yield of the XBP

$$ \begin{aligned} Y_{\rm VI} &\equiv \int_0^R {\rm d}r \int {\rm d}N(W){\rm d}W \\ &= 2\pi\kappa g\eta\rho L \int_0^R r{\rm d}r \int n_{\rm r}(W){\rm d}W \\ &= 2\pi\kappa g\eta\rho L \int_0^R r{\rm d}r Y_{\rm SI} \\ &= \pi\kappa g\eta\rho L R^2 Y_{\rm SI}. \end{aligned} \tag{6} $$

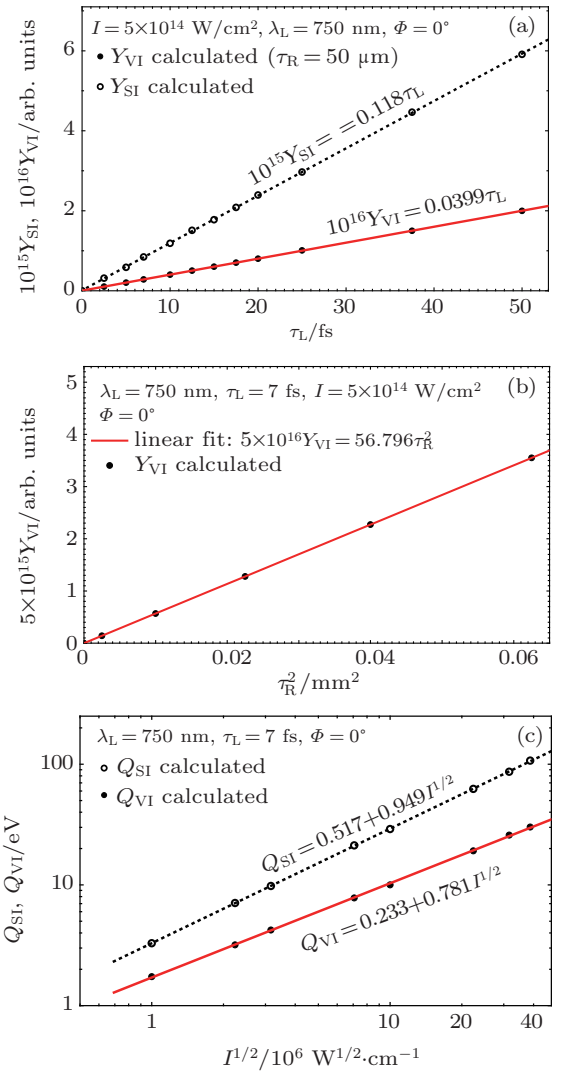



**Fig. 5.** (color online) PES statistical properties. (a) Open (filled) circles: $Y_{\rm SI}$ ($Y_{\rm VI}$) versus $\tau_{\rm L}$. The dotted (solid) line is linearly fitted from $Y_{\rm SI}$ ($Y_{\rm VI}$). (b) Filled circles: $Y_{\rm VI}$ versus $\tau_{\rm R}^2$. The solid line is linearly fitted from $Y_{\rm VI}$. (c) Open (filled) circles: $Q_{\rm SI}$ ($Q_{\rm VI}$) versus $I^{1/2}$. The dotted (solid) line is linearly fitted from $Q_{\rm SI}$ ($Q_{\rm VI}$).

Note that $Y_{VI} \propto Y_{SI}$, $Y_{VI} \propto \tau_L$ (because of $Y_{SI} \propto \tau_L$), $Y_{VI} \propto LR^2$, and $Y_{VI}$ is a constant for different values of $I$ and $\Phi$. Because $R$ is proportional to $\tau_R$, we have $Y_{VI} \propto \tau_R^2$. The factor $\pi\kappa g\eta\rho LR^2$ disappears in the expression of $Q$ due to the normalization by $Y$ (Eq. (3)). Our calculations also show that: (i) both SI $Q$ ($\equiv Q_{SI}$) and VI $Q$ ($\equiv Q_{VI}$) are independent of $\Phi$, (ii) $Q_{VI}$ is independent of $\tau_R$, (iii) $Q_{SI}$ and $Q_{VI}$ depend very weakly on $\tau_L$ (e.g., $Q_{SI} = 59.990$–$63.803$ eV, $Q_{VI} = 18.549$–$19.379$ eV for $\tau_L = 2.5$–$50$ fs and $I = 5 \times 10^{14}$ W/cm$^2$), and (iv) $Q_{SI}$ and $Q_{VI}$ are proportional to $I^{1/2}$.

Figures 5(a)–5(c) present some statistical properties of the PES. Figure 5(a) shows $Y_{SI}$ ($Y_{VI}$) versus $\tau_L$. Figure 5(b) presents $Y_{VI}$ versus $\tau_R^2$. Figure 5(c) presents $Q_{SI}$ ($Q_{VI}$) versus $I^{1/2}$. All of the data can be fitted with linear curves. A quantitative analysis of these statistical properties shows that the XBP production $Y$ and the $Q$ value linearly and sensitively depend on $\tau_L\tau_R^2$ and $I^{1/2}$, respectively. These linear relations (calibrated with values retrieved from the SI fingerprint data) can be used to quickly determine $\tau_L$, $I$, and $\tau_R$ in experiments.

### 3.1. PES energy differences

Figures 6(a) and 6(b) show VI $y(W)$ near 0 and 1 for different CEPs $\Phi$ from 0° to 360°. The curves for 0° and 180° (45° and 135°, 90° and 270°) are the same. The insets in Figs. 6(a) and 6(b) show the expanded plots for $y(W)$ close to 0 and 1, respectively. The plots clearly demonstrate that $y(W)$ twists tightly in some energy regions (e.g., the two regions denoted by the dotted circles $C1$ and $C2$) and loosely in other regions. As $\tau_L$ increases, the calculated curve $y(W)$ becomes smoother, and the curves of $y(W)$ for different $\Phi$ become more tightly twisted. The open (filled) triangles in Fig. 6(c) present the VI values corresponding to $W_{0.01}$ ($W_{0.99}$) versus $I^{1/2}$, where $y(W_{0.01}) = 0.01$ ($y(W_{0.99}) = 0.99$). The open (filled) circles show the SI (VI) values corresponding to the energy differences $\Delta W_{SI}$ ($\Delta W_{VI}$) $\equiv W_{0.99} - W_{0.01}$. The lines are linearly fitted to the data. The linear relationships between $\Delta W_{SI,VI}$ and $I^{1/2}$ can be used to determine the laser intensity $I$ from the energy differences $\Delta W_{SI,VI}$ for specified $y(W)$ values.

Tables 1–5 show some VI data corresponding to $W_{0.01}$, $W_{0.99}$, $\Delta W_{VI} = W_{0.99} - W_{0.01}$, $\delta W_{VI} \equiv \Delta W_{VI} - \overline{\Delta W}_{VI}$, $\delta_{VI} \equiv \delta W_{VI}/\overline{\Delta W}_{VI}$, which are calculated with $\lambda_L = 750$ nm, $\tau_L = 7$ fs, $\omega_X = 1$ keV, $I = 10^{12}$–$1.5 \times 10^{15}$ W/cm$^2$, and $\Phi = 0°$–$360°$. Here, $\overline{\Delta W}_{VI}$ is the mean value of the calculated energy differences. Calculations with $I = 10^{12}$, $10^{13}$, $10^{14}$, $5 \times 10^{14}$, $10^{15}$ (W/cm$^2$) give the mean values of $\overline{\Delta W}_{VI} = 32.619$, 86.397, 238.049, 496.188, 692.360 (eV) for $\Phi = 0°$–$360°$, differences of $|\delta W_{VI}| < 0.043$, 0.457, 0.978, 2.817, 4.901 (eV), and relative differences of $|\delta_{VI}| < 0.132\%$, 0.529%, 0.411%, 0.568%, 0.708%, respectively. Calculations with different pulse durations $\tau_L$ produce similar results, which suggests that the laser intensity $I$ can be determined from the VI data of $\Delta W_{VI}$ versus $I^{1/2}$. This $I$ value can be used to calibrate the linearity of $Q_{VI}$ versus $I^{1/2}$.

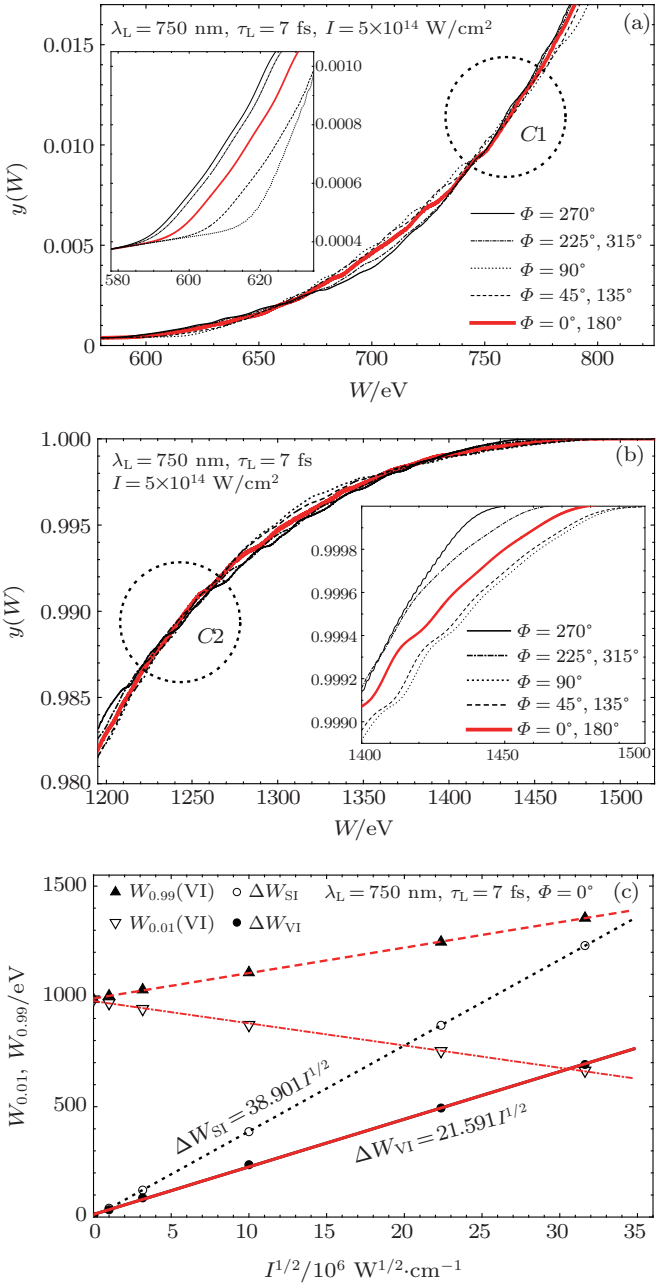



**Fig. 6.** (color online) (a) and (b) Normalized and energy-integrated VI XBP PES, $y(W) = \int_{W_{a-}}^{W} dW' n(W')/Y$. (a) Lines: $y(W)$ at low energies calculated for $\Phi = 0°$–$360°$. Inset: an expanded plot for $y(W)$ close to 0. (b) The $y(W)$ at high energies. Inset: an expanded plot for $y(W)$ close to 1. (c) PES energy properties. Open (filled) triangles: VI data corresponding to $W_{0.01}$ ($W_{0.99}$) versus $I^{1/2}$. Open (filled) circles: SI (VI) data corresponding to $\Delta W_{SI}$ ($\Delta W_{VI}$) $\equiv W_{0.99} - W_{0.01}$ versus $I^{1/2}$.

**Table 1.** VI data calculated with $I = 10^{12}$ W/cm$^2$ and $\overline{\Delta W}_{VI} = 32.619$ eV.

| $\Phi$ | $W_{0.01}$/eV | $W_{0.99}$/eV | $\Delta W_{VI}$/eV | $\delta W_{VI}$/eV | $\delta_{VI}$/% |
|---|---|---|---|---|---|
| 0° | 969.955 | 1002.566 | 32.612 | –0.007 | –0.025 |
| 45° | 970.017 | 1002.611 | 32.594 | –0.025 | –0.076 |
| 90° | 970.035 | 1002.644 | 32.609 | –0.010 | –0.030 |
| 135° | 970.017 | 1002.611 | 32.594 | –0.025 | –0.076 |
| 180° | 969.955 | 1002.566 | 32.612 | –0.007 | –0.022 |
| 225° | 969.894 | 1002.532 | 32.637 | 0.019 | 0.057 |
| 270° | 969.852 | 1002.514 | 32.662 | 0.044 | 0.133 |
| 315° | 969.894 | 1002.531 | 32.637 | 0.019 | 0.057 |
| 360° | 969.955 | 1002.566 | 32.612 | –0.007 | –0.022 |

**Table 2.** VI data calculated with $I = 10^{13}$ W/cm$^2$ and $\overline{\Delta W}_{\rm VI} =$ 86.397 eV.

| $\Phi$ | $W_{0.01}$/eV | $W_{0.99}$/eV | $\Delta W_{\rm VI}$/eV | $\delta W_{\rm VI}$/eV | $\delta_{\rm VI}$/% |
|---|---|---|---|---|---|
| 0° | 943.236 | 1029.976 | 86.740 | 0.342 | 0.396 |
| 45° | 942.622 | 1029.036 | 86.415 | 0.017 | 0.020 |
| 90° | 942.520 | 1028.460 | 85.940 | –0.457 | –0.529 |
| 135° | 942.621 | 1029.036 | 86.415 | 0.018 | 0.020 |
| 180° | 943.236 | 1029.976 | 86.740 | 0.342 | 0.396 |
| 225° | 943.988 | 1030.263 | 86.275 | –0.123 | –0.142 |
| 270° | 944.548 | 1030.586 | 86.038 | –0.359 | –0.415 |
| 315° | 943.989 | 1030.263 | 86.274 | –0.123 | –0.142 |
| 360° | 943.236 | 1029.976 | 86.740 | 0.342 | 0.396 |

**Table 3.** VI data calculated with $I = 10^{14}$ W/cm$^2$ and $\overline{\Delta W}_{\rm VI} =$ 238.049 eV.

| $\Phi$ | $W_{0.01}$/eV | $W_{0.99}$/eV | $\Delta W_{\rm VI}$/eV | $\delta W_{\rm VI}$/eV | $\delta_{\rm VI}$/% |
|---|---|---|---|---|---|
| 0° | 870.830 | 1107.944 | 237.114 | –0.935 | –0.393 |
| 45° | 868.901 | 1107.688 | 238.787 | 0.738 | 0.310 |
| 90° | 869.131 | 1107.765 | 238.634 | 0.585 | 0.246 |
| 135° | 868.900 | 1107.688 | 238.788 | 0.739 | 0.310 |
| 180° | 870.830 | 1107.945 | 237.115 | –0.934 | –0.393 |
| 225° | 870.830 | 1107.945 | 237.115 | –0.934 | –0.393 |
| 270° | 871.187 | 1109.934 | 238.748 | 0.699 | 0.294 |
| 315° | 871.269 | 1110.296 | 239.028 | 0.979 | 0.411 |
| 360° | 870.830 | 1107.944 | 237.114 | –0.935 | –0.393 |

**Table 4.** VI data calculated with $I = 5 \times 10^{14}$ W/cm$^2$ and $\overline{\Delta W}_{\rm VI} =$ 496.188 eV.

| $\Phi$ | $W_{0.01}$/eV | $W_{0.99}$/eV | $\Delta W_{\rm VI}$/eV | $\delta W_{\rm VI}$/eV | $\delta_{\rm VI}$/% |
|---|---|---|---|---|---|
| 0° | 752.679 | 1246.656 | 493.977 | –2.211 | –0.446 |
| 45° | 749.072 | 1248.071 | 498.999 | 2.811 | 0.567 |
| 90° | 750.011 | 1247.904 | 497.893 | 1.705 | 0.344 |
| 135° | 749.067 | 1248.072 | 499.005 | 2.817 | 0.568 |
| 180° | 752.671 | 1246.657 | 493.987 | –2.201 | –0.444 |
| 225° | 752.024 | 1247.180 | 495.156 | –1.032 | –0.208 |
| 270° | 751.923 | 1249.470 | 497.547 | 1.359 | 0.274 |
| 315° | 752.029 | 1247.180 | 495.151 | –1.037 | –0.209 |
| 360° | 752.679 | 1246.656 | 493.977 | –2.211 | –0.446 |

**Table 5.** VI data calculated with $I = 10^{15}$ W/cm$^2$ and $\overline{\Delta W}_{\rm VI} =$ 692.360 eV.

| $\Phi$ | $W_{0.01}$/eV | $W_{0.99}$/eV | $\Delta W_{\rm VI}$/eV | $\delta W_{\rm VI}$/eV | $\delta_{\rm VI}$/% |
|---|---|---|---|---|---|
| 0° | 663.876 | 1355.088 | 691.212 | –1.148 | –0.166 |
| 45° | 659.433 | 1356.664 | 697.230 | 4.870 | 0.703 |
| 90° | 663.876 | 1355.088 | 691.212 | –1.148 | –0.166 |
| 135° | 659.404 | 1356.665 | 697.261 | 4.901 | 0.708 |
| 180° | 663.832 | 1355.090 | 691.257 | –1.102 | –0.159 |
| 225° | 663.122 | 1352.087 | 688.964 | –3.396 | –0.491 |
| 270° | 663.965 | 1357.924 | 693.959 | 1.600 | 0.231 |
| 315° | 663.155 | 1352.086 | 688.931 | –3.429 | –0.495 |
| 360° | 663.876 | 1355.088 | 691.212 | –1.148 | –0.166 |

## 4. Conclusion

The field modulation and the strong quantum interference of the X-ray-boosted photoionization collaboratively produce interesting and useful statistical properties. (i) Both the SI and VI XBP's production $Y$ values are invariants for different CEPs $\Phi$ and are slow variables for different laser intensities $I$. (ii) The XBP's $Q$ value is independent of CEP $\Phi$, laser pulse duration $\tau_{\rm L}$, and beam size $\tau_{\rm R}$ (FWHM). (iii) Both the SI and VI $Y$ values linearly and sensitively depend on the product of the pulse duration $\tau_{\rm L}$ and the square of the beam size $\tau_{\rm R}$, namely, $Y \propto \tau_{\rm L}\tau_{\rm R}^2$. (iv) The $Q$ value is an intrinsic value of the XBP spectrum, which quantitatively reflects the strength of the field modulation and the quantum interference. Both SI and VI $Q$ values linearly and sensitively depend on $I^{1/2}$; that is, $Q \propto I^{1/2}$.

The precise *in-situ* measurement of an intense laser pulse can be achieved using a simplified algorithm with a measured PES. The parameters $\tau_{\rm L}$, $\Phi$, and $I$, which are retrieved from the SI fingerprint data, can be used to calibrate the linearities of the XBP energetic and statistical properties for both SI and VI measurements.

Although the simulations are performed with $I < 10^{16}$ W/cm$^2$, the methods can work with $I$ up to $10^{18}$ W/cm$^2$ by using higher-energy X-rays and highly charged inert gases. These methods have also inspired us to address measurements with $I > 10^{18}$ W/cm$^2$, where the Lorentz force plays a role in the motion of photoelectrons.

## References


[1] Ge Y C and He H P 2014 *Chin. Phys. B* **23** 074207
[2] Bula C, McDonald K T, Prebys E J, Bamber C, Boege S, Kotseroglou T, Melissinos A C, Meyerhofer D D, Ragg W, Burke D L, Field R C, Horton-Smith G, Odian A C, Spencer J E, Walz D, Berridge S C, Bugg W M, Shmakov K and Weidemann A W 1996 *Phys. Rev. Lett.* **76** 3116
[3] Chang Z, Rundquist A, Wang H, Murnane M M and Kapteyn H C 1997 *Phys. Rev. Lett.* **79** 2967
[4] Perry M D and Mourou G 1994 *Science* **264** 917
[5] Mashiko H, Suda A and Midorikawa K 2004 *Opt. Lett.* **29** 1927
[6] Lewenstein P, Balcou P, Ivanov M Y, L'Huillier A and Corkum P B 1994 *Phys. Rev. A* **49** 2117
[7] Ge Y C 2008 *Chin. Phys. B* **17** 4492
[8] Wiehle R, Witzel B, Helm H and Cormier E 2003 *Phys. Rev. A* **67** 063405
[9] Agostini P, Fabre F, Mainfray G, Petite G and Rahman N K 1979 *Phys. Rev. Lett.* **42** 1127
[10] Guo D S 2013 *Phys. Rev. Lett.* **110** 063002
[11] Ge Y C 2006 *Phys. Rev. A* **74** 015803
[12] Ge Y C 2008 *Phys. Rev. A* **77** 033851
[13] Ge Y C and He H P 2011 *Phys. Rev. A* **84** 023804
[14] Ge Y C 2008 *Chin. Phys. B* **17** 2072
[15] Ge Y C 2009 *Chin. Phys. B* **18** 1473